A MultiScale Algorithm for Nuclei Extraction in Pap Smear Images.

Dibet Garcia-Gonzalez, Miguel Garcia-Silvente, Eugenio Aguirre

Department of Computer Science and Artificial Intelligence, Centro de Investigación en Tecnologías de La Información y de las Comunicaciones (CITIC), University of Granada, 18071 Granada, Spain.
Emails: dibet@decsai.ugr.es, m.garcia-silvente@decsai.ugr.es, eaguirre@decsai.ugr.es

Abstract

This work presents a new automated method which manages multiscale information and combines segmentation and classification algorithms for nuclei extraction in pap smear images. The accuracy of the segmentation algorithms was evaluated using the comparison functions relative distance error and object consistency error. The harmonic mean of sensitivity and specificity was used in the classification evaluation. The evaluation of different alternatives shows as the best result the combination of the Shape Detection and Artificial Neural Network. The multiscale approach provides a convenient way to combine information from different resolutions. It outperforms the usual algorithms because there is no single "true" scale for a Pap smear images. The proposal is fast enough and accurate and, so, it is very helpful for cell screening. Usually, the algorithms that include as one of their steps the classification of information, do not justify the choice made. On this work a study is included on which is the best classification method for the Nuclei Extraction in Pap Smear Images.

Key words: biomedical imaging, image segmentation, multiresolution analysis, ellipse fitting, cell screening, classification algorithms, cervical cancer diagnosis

1. Introduction

The feature extraction is a task that appears very frequently on the area of application of the expert and intelligent systems, such as image processing or bioinformatics. For the feature extraction it is necessary to consider the relevant characteristics and differentiate them from the ones that are not (Bennasar et al., 2015). On the other hand, an interesting approach to the classification problem consists to perform an evaluation of the different classification methods that could be relevant to the problem (Gerlein et al., 2016).

Cervical cancer is one of the most common cancers that affects women (Lassouaoui et al., 2005). Its early detection contributes to the total cure of the disease. So, prevention plays an important role in its treatment. This is done by cytological evidence which may contain thousands of cells per tested sample (Papanicolaou test). The analysis of the microscopy slides is usually carried out by cytotechnicians in specialized laboratories under the supervision of a pathologist. A main part of the diagnostic process normally consists of categorizing the slide according to the Bethesda 2001 system(WorldHealthOrganization, 2006). Many of the anomalies a cytotechnician looks for, that are the base for this categorization, are characteristics of the cell nuclei (i.e. their shape, colour, size, proportion to cytoplasm and so on). So, an automatic analysis system of cervical cell images has to perform a process of segmentation, feature extraction, classification, validation, and error management.

This process is highly repetitive and may be subject to a lot of human mistakes. For this reason, the development of computer systems that automate the process of analysis of these samples has an important place in the area of computer vision. The main objective of such systems is to show the pathologists the diseased cells in a sample containing diseased and healthy cells, and therefore to eliminate the need to examine all the cells in the sample.

The slides typically contain thousands of cells. They are scanned with a maximum magnification level of 40x, which results in large digitized files with a size around 80.000 pixels in each dimension. Different magnification levels are used for different tasks, such as background and overall slide quality identification, analysis of cell groupings and clusters, or determination of single cell characteristics

So far, several studies have been performed but they still do not reach

the quality required for a reliable medical application. In (Harandi et al., 2010) a new segmentation method is proposed, it firstly finds cell objects in low resolution [1]. Next, in high resolution, then the algorithm extracts the nuclei and cytoplasm contour using the geometric active contours level set. In order to correct the results, an automatic circular decomposition method is adapted. In (Sagiv et al., 2006) the texture information is used for guiding the contour deformation. Another approximation(Pai et al., 2012) uses the adaptable threshold decision (ATD) method to separate the cell from the cervical smear image, and then proposes the use of the maximal grey-level-gradient-difference (MGLGD).

The technique proposed in (Lin et al., 2009) starts with an equalization and Gaussian filter for noise reduction. Next, the average value of coarseness calculation for each pixel, which is later used as a determining characteristic of reinforced object images. A two-group object enhancement technique is then used to reinforce this object according to rough pixels Finally, an edge detection like Sobel filter with some post processing, and noise elimination in the results is done. In (Vaschetto et al., 2009) a fuzzy system which integrates colour information and cytopatologists knowledge is developed for the nuclei segmentation. The hue, saturation and intensity (HSI) colour space is used.

In (Ali et al., 2012) a texture based segmentation is performed. The idea is to consider the orientation of the cell contours and, then a level-set fitting. The information is considered in a coarser scale.

In (Lassouaoui et al., 2005), a genetic algorithm is used for nuclei and cytoplasm segmentation. In order to improve the segmentation, the identified areas are classified under the Fisher algorithm (González and Goods, 2002). In (Kim et al., 2007) the HSI model is used for the nucleus region extraction from an image of uterine cervical cytodiagnosis. Firstly, a preprocessing step to eliminate noise in the image is made. Then, mathematical morphology is applied, with a fuzzy kernel of size 5 by 5, in order to correct the effect of the noise elimination and to allow the accurately extraction of the nuclei of the cells. Finally, an iterative threshold selection method is applied for nucleus extraction.

Also, morphological analysis has been used in order to detect the nuclei centroids (Plissiti et al., 2011b). Afterwards, the clustering is used and is compared with fuzzy C-means and SVM. A priori information about the

---

[1]Scaling each image at 25% with bilinear interpolation method.

circumference of each nucleus is used.

Graph cut-based algorithms are also used(Zhang et al., 2014) in order to segment the images. In this work, several straightforward preprocessing techniques are performed and then, the graph cut-based algorithm is applied.

In (Malm et al., 2013), a sequential classification scheme focused on removing unwanted objects, debris, from an initial segmentation result is proposed. It is intended to be run before the actual normal/abnormal classifier. Authors claim that they achieve a 99% percent removal of debris.

There are another solutions in which ellipses are searched(Bergmeir et al., 2012) but the use of only one scale limits the accuracy of the results.

Recently, Farhan et al(Farhan et al., 2013) used a multi-scale Gaussian representation but the scales considered were very overlapped and the way to perform the combination were not much effective.

Hough Transform (HT) is considered a standard in curve detection(Inverso, 2002). Its main drawback is the performance in time. In order to solve this problem, two alternatives were proposed: Randomized Hough Transform (RHT) and Probabilistic Hough Transform (PHT). Xu(Xu et al., 1990) states that RHT cannot be used for 'curves expressed by equations which are non-linear with respect to parameters', which includes ellipses. Robert McLaughlin(McLaughlin, 1998) experimented with RHT and compared it against the standard HT and Probabilistic Hough Transform (Probabilistic Hough Transform is similar to Hough Transform but only a small portion α of the pixels in the image, where $2\% < \alpha < 15\%$, are transformed).

Our proposal outperforms the different variants of HT when applied to this problem since our algorithm performs a fast smoothing in parameter space and, also a fast ellipse calculation based on very few points. Other very recent work(Li et al., 2012) uses a particular kind of Snakes, the Radiating GVF Snake.

Other works, like (Oliver et al., 1979), (Koss et al., 1997), (Colantonio et al., 2008), (Sobrevilla et al., 2008), (Mat-Isa et al., 2008),(Chen et al., 2003),(Plissiti et al., 2011a) propose systems for cervix cell segmentation.

Our proposed algorithm takes advantage of: multiscale edge detectors, ellipse parameter calculation, segmentation algorithms based on level set and classification algorithms. Multiscale detectors are considered among the most robust in the presence of noise and when accuracy is relevant. The nuclei can be approximated by ellipses and its centre determined from incomplete edges. Segmentation algorithms allow, from the centre of the ellipse detected, to find the real edges of the nuclei. Finally, classification techniques are used

to discriminate between true and false nuclei.

2. Proposed method

The proposed algorithm has 4 major steps: preprocessing, estimating of the centre of the nucleus, segmenting the nucleus region and discrimination between nucleus and no nucleus. Fig. 1 shows a block diagram of the algorithm that will be detailed below.
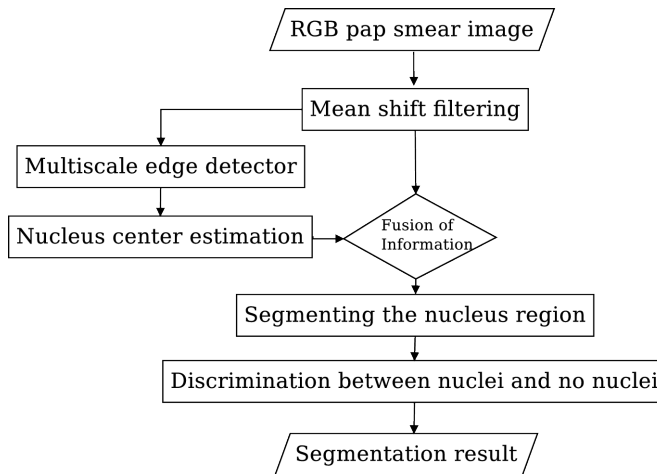

Figure 1: Block diagram of the proposed algorithm

2.1. Preprocessing

The preprocessing step is divided in two parts. The first part consists in applying a mean-shift filter based on mean-shift clustering over colour (Comaniciu and Meer, 1999). Afterwards, we use a variant of a multiscale edge detector(Garcia-Silvente et al., 1997) based on the Canny edge detector (Canny, 1986). The used edge detector has the advantage of considering the scale in which information can be processed in a more suitable way. The algorithm determines with accuracy the edge spatial localization in the original image and, at the same time, it eliminates both noise and unnecessary detail from appearing on the image. Moreover, the edges are not fragmented and the sharp changes in grey level are not smoothed except for those cases in which changes are best defined for a higher scale. The algorithm is based on the use of *stable areas* for every edge point. Those areas correspond to

5

the place where an edge point could be located if it moves "in a stable way" to the following scale(Garcia-Silvente et al., 1997). The algorithm can be reviewed in Algorithm 1

Algorithm 1 Multiscale edge points calculation

Require: SA (set of "stable edges" for every considered point and scale($1,2,...2^n$))
Ensure: I_{final}
  $I_{final} \Leftarrow \emptyset$
  for $k = 1$ **to** number of scales/2+1 **do**
    for each (x_1, x_2) such that (x_1, x_2) in the initial image **do**
      p $\Leftarrow \max\{1, \text{number of scales/2}\}$
      if $(x_1, x_2) \notin SA_{(x_1,y_1)_{k-1}}$ **and** $(x_1, x_2) \in SA_{(x_1,y_1)_k}$ **and** to a series
          $SA_{(x_2,y_2)_{k+1}},\cdots,SA_{(x_{p+1},y_{p+1})_{k+p-1}}$ **then**
        $A \Leftarrow \{(m, n)/(x_1, x_2) \in SA_{(m,n)_k}\}$
        $I_{final} \Leftarrow I_{final} \cup A$
      end if
    end for
  end for

Fig. 2 shows the results of applying the preprocessing.

2.2. Estimating the centre of the nuclei

In order to perform the initial estimation of the centre of the cell nucleus (x_{nc},y_{nc}), it is assumed that the outline of the nuclei can be approximated by an ellipse. Ellipses have the property that their parameters: centre (x_{ec},y_{ec}), semi-major axis (a), semi-minor axis (b) and angle of inclination of the semi-major axis relative to the axis of coordinates $(angle)$ can be calculated from three points belonging to the edge of the ellipse (x_a, y_a), (x_b, y_b) and (x_c, y_c) as shown in Fig. 3. r_a, r_b and r_c are the tangents to the ellipse and passing through points (x_a, y_a), (x_b, y_b) and (x_c, y_c) respectively; (x'_{ab}, y'_{ab}) and (x'_{bc}, y'_{bc}) are the points of intersection of lines r_a and r_b, and r_b and r_c respectively; (x_{ab}, y_{ab}) and (x_{bc}, y_{bc}) are the midpoints between the points (x_a, y_a) and (x_b, y_b), and (x_b, y_b) and (x_c, y_c) respectively. Then the centre of the ellipse (x_{ec},y_{ec}) is determined by the intersection of the lines through points (x'_{ab}, y'_{ab}) and (x_{ab}, y_{ab}) and points (x'_{bc}, y'_{bc}) and (x_{bc}, y_{bc}) .
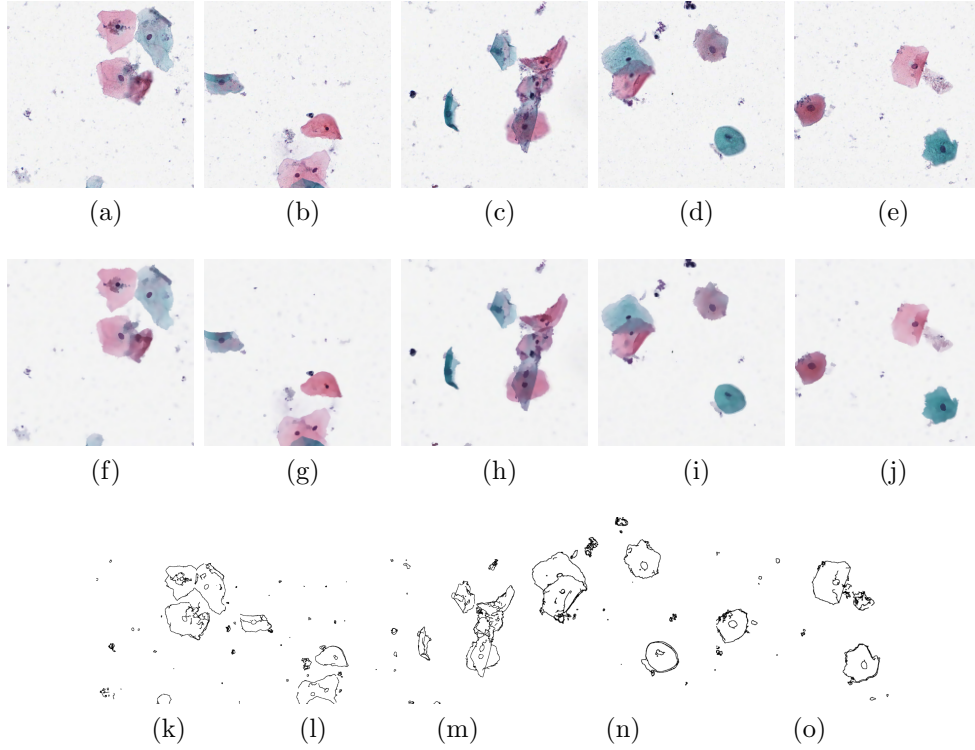
6

Figure 2: (a-e) Original images. (f-j) Mean shift segmentation. (k-o) Multiscale edge detector
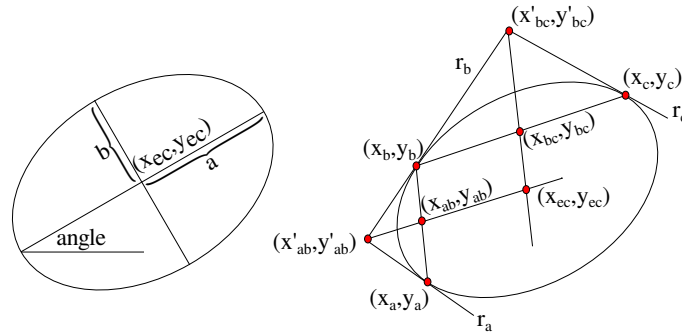

Figure 3: Estimation of ellipse parameters using three candidate points of the contour

The proposed algorithm covers the whole image with a square sliding window of size $S \times S$ as shown in the Fig. 4. Taking into consideration the size range that can reach a cell nucleus, it was decided to adjust $S = 2r_{min} + r_{max}$

and $s = r_{min}$. Where r_{min} and r_{max} are considered as the minimum and maximum sizes that can be reached by the cell nuclei.
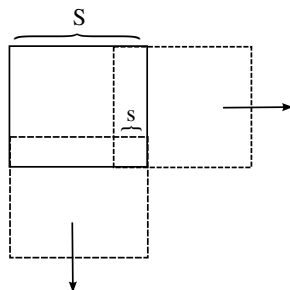

Figure 4: Square sliding window for covering the whole image

In every window, three points are randomly selected, N times. For each triad of points, the centre of the ellipse is determined, and also the dimensions of the semi-axes and the inclination angle. From these data, for each N possible centres, we select all the pixels in the image edges between 40% and 110% of the semi-axis of the ellipse as shown in the blue area of the Fig. 5.
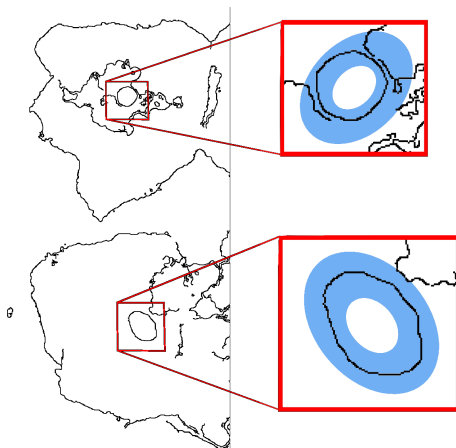

Figure 5: Selection of the candidate points, the blue area represents the space in which the pixels are selected for next step

From all the pixels that are in the blue area, three points, M times, are randomly selected and then a search for the ellipse centre is performed. Each calculated centre taxed at an array of votes M_V. The algorithm scans

the array of possible votes and selects as seed point (x_s, y_s) the one that maximizes the Eq. 1 in a neighbourhood of size $5x5$.

$$V(x_s, y_s) = \sum_{y=y_s-2}^{y_s+2} \sum_{x=x_s-2}^{x_s+2} M_v(x,y) exp(-\frac{\sqrt{(x_s-x)^2+(y_s-y)^2}+\mu}{\sigma^2}) \quad (1)$$

Where $\mu = 0$ and $\sigma = 1$. Fig. 6 shows an example where the sum reaches maximum value of 91.8786.

$V(x_s, y_s$ calculates the maximum considering the neighbourhood of every point. The goal of this is to avoid the clustering problem associated to the use of voting.

	1	2	3	4	5
1	0	2	4	2	0
2	2	4	18	4	2
3	2	12	38	14	4
4	4	6	24	10	2
5	0	4	8	4	2

Figure 6: Example of the application of Eq. 1 using a $5x5$ vote window, with a calculated maximum value of 91.8786

After finding a maximum of N possible seed points (x_s, y_s), the most voted are selected. If the highest voted point exceeds a certain threshold, it is selected as a possible centre of a nucleus (x_{nc}, y_{nc}) for further processing. This centre serves as a seed in a subsequent step that will find the real edges of the cell nucleus. After finding the nucleus edges, every pixel of the image edges that matches the selected nucleus is removed from the image in order to avoid considering the same centre twice. This process is repeated while there are sensing centres in the sliding window.

Fig. 7 shows the Multiscale edge image with the centres that have been identified in red.

At every axis, the selection of three points, from which the ellipses are detected, is performed as follows:

- First point $p_a(x_a, y_a)$. From all points of the image, one is randomly selected.

- Second point $p_c(x_c, y_c)$. From the remaining points, one is randomly selected, so that the minimum Euclidean distance to the first point must be between r_{min} and r_{max}.
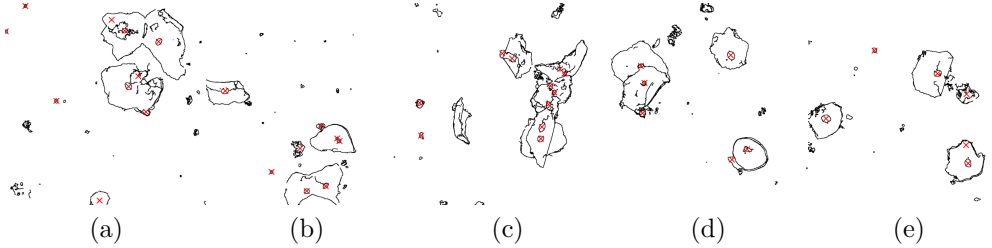
Figure 7: (a-e) Centres detected from the Multiscale edge image

- Third point $p_b(x_b, y_b)$. From the points identified above, the third point is randomly selected if it is in the green region as shown in Fig. 8 where $(p_m(x_m, y_m))$ is the midpoint between points p_a and p_c.
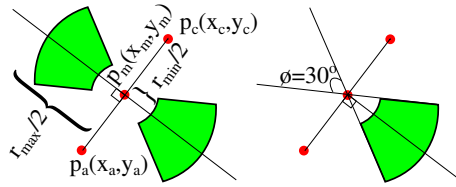

Figure 8: Selection of ellipse points, the green region represents the area where the third pixel is randomly selected

2.3. Segmenting the nuclei region

From the given seed point (x_s, y_s) in the previous step, we proceed to find the best approximation of the edges of the nuclei. Firstly, those points are removed from the multiscale edge image in order to avoid finding the same centre several times and also to achieve a rapid convergence of the algorithm. Starting from the mean shift image that was previously calculated and the seed points in the previous stage, six algorithms are applied to find the actual edges of the nuclei.

2.3.1. Segmentation algorithms

The considered algorithms are the following:

10

- Fast marching (FM)

  Fast marching is an algorithm that uses differential equations with a very simple form to govern the level set evolution(Ibanez et al., 2003). The differential equation is typically computed as a function of the gradient magnitude. The mapping should be done in such a way that the propagation speed of the front will be very low close to high image gradients while it will move rather fast in low gradient areas. The output of the Fast Marching is a time-crossing map that indicates, for each pixel, how much time it would take for the front to arrive at the pixel location. Segmentation is performed with this filter by locating a time range in which the contour was contained for long time in a region of the image space. The main advantage of using level set is that it can model complex shapes. Moreover, topological changes such as mix and divisions are implicitly handled.

- Shape detection (SD)

  This algorithm was proposed in (Malladi et al., 1995). In this algorithm, the differential equation that governs the evolution of the level set, includes a curvature-based term. Its main function is to soften areas of large curvature that are assumed as due to noise. Its first step is to perform a Fast Marching filter.

- Geodesic active contour (GAC)

  Proposed in (Caselles et al., 1997), this algorithm is an extension of Shape Detection (SD). It adds a third advection term which attracts the level set to the object boundaries. So propagation, curvature and advection terms are considered.

- Watershed (WS)

  This algorithm was proposed in (Meyer and Beucher, 1990). Watershed segmentation classifies pixels into regions using gradient descent on image features and analysis of weak points along region boundaries. The algorithm considers the image as a set of mountains and valleys and it is similar to the effect of flooding little by little.

- Region growing connected threshold (RGCT)

  From a seed point (x_s, y_s), which is considered to be within the target object, the pixels are evaluated to determine if their neighbourhood

11

belongs to the object being segmented. If the pixel considered belongs to the object of interest, it is added to the resulting region. The process will continue as long as pixels to the result are added.

The criterion for judging whether the pixel (x, y) belongs to the neighbourhood (8 connected) resulting region, is based on a current value range (Th) provided by the user. With the seed point, the intensity value is determined, $I(x_s, y_s)$, and the pixels will be considered as neighbourhood if meet the following condition:

$$[I(x_s, y_s) - Th < I(x, y) < I(x_s, y_s) + Th] \tag{2}$$

- Region growing neighbourhood connected (RGNC).

  This algorithm is a variant of the above(Ibanez et al., 2003). It only accepts a pixel in the region if all its neighbours within a certain radius satisfy the condition of the Eq. 2.

2.3.2. Comparison functions for the evaluation of the segmentation results

The segmentation results of each of these algorithms are evaluated using the comparison function Relative Distance Error (RDE) (Yang-Mao et al., 2008) and Object Consistency Error (OCE) (Polak et al., 2009):

- Relative Distance Error (RDE)

  RDE is calculated as:

$$RDE = \frac{1}{2} \left(\sqrt{\frac{1}{n_e} \sum_{i=1}^{n_e} d_{e_i}^2} + \sqrt{\frac{1}{n_t} \sum_{j=1}^{n_t} d_{t_j}^2} \right) \tag{3}$$

  Where $d_{t_j} = min\{dist\,(e_i, t_j)\,|i = 1, 2, \ldots, n_e\}$ and $d_{e_i} = min\{dist\,(e_i, t_j)\,|j = 1, 2, \ldots, n_t\}$. $e_1, e_2, e_3, \ldots, e_{n_e}$ are the SR pixels (in the Selected Region) and $t_1, t_2, t_3, \ldots, t_{n_t}$ are the GT pixels; n_e and n_t are the number of pixels of SR and GT respectively; $dist\,(e_i, t_j)$ represents the euclidean distance between e_i and t_j.

- Object Consistency Error (OCE)

  OCE is a comparison function that penalizes the over and under segmentation. It begins by defining a partial error measure as:

$$E_{g,s}(I_g, I_s) = \sum_{j=1}^{M} \left[1 - \sum_{i=1}^{N} \frac{|A_j \bigcap B_i|}{|A_j \bigcup B_i|} \times W_{ji} \right] W_j \tag{4}$$

$$W_{ji} = \frac{\overline{\delta}(|A_j \bigcap B_i|)|B_i|}{\sum_{k=1}^{N} \overline{\delta}(A_j \bigcap B_k|)|B_k|)} \tag{5}$$

$$W_j = \frac{|A_j|}{\sum_{l=1}^{M} |A_l|} \tag{6}$$

Where I_g y I_s are the GT and the SR. M and N are the number of regions that exists in I_g and I_s, respectively. A_i represents the ith region in I_g. B_j represents the jth region in I_s. $\delta(x)$ is the delta function whose value is 1 if the input is zero, else is zero. $\overline{\delta}(x) = 1 - \delta(x)$

$$OCE = \min(E_{g,s}, E_{s,g}) \tag{7}$$

2.3.3. Comparison

With these results we constructed two frequency histogram which are shown in Figs. 9 and 10.
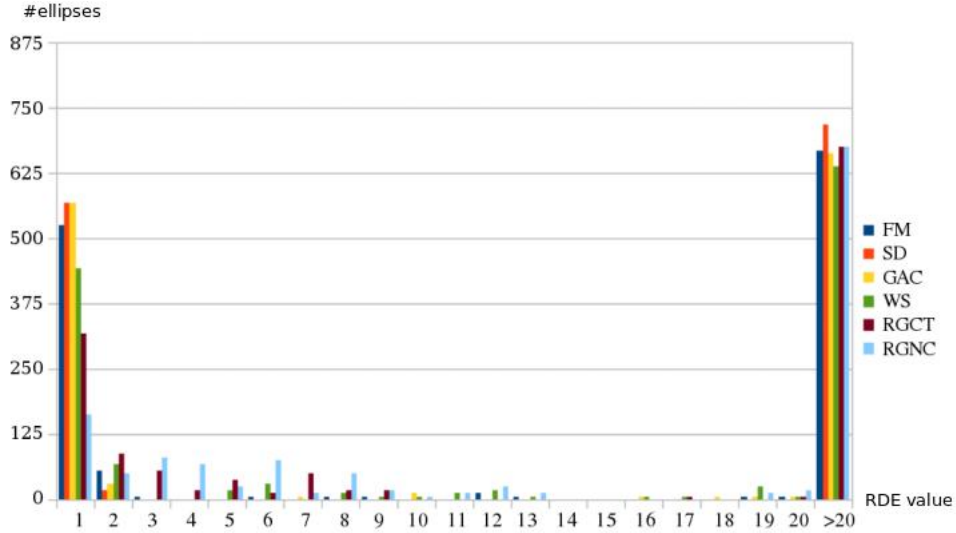

Figure 9: Frequency histogram of the results of RDE for the six segmentation methods
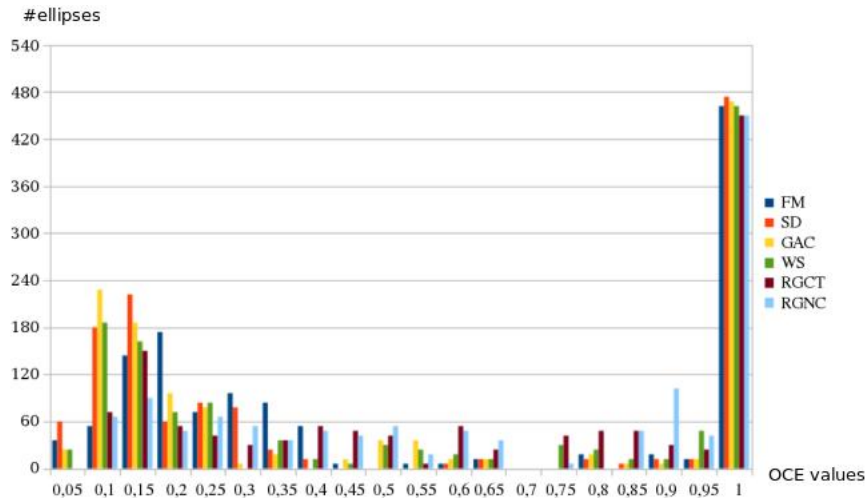
13

Figure 10: Frequency histogram of the results of OCE for the six segmentation methods

On Fig. 9 we see two trends for each segmentation algorithm. Values near zero indicate a result very close to the Ground Truth (GT) and higher levels mean that the segmentation result does not match the GT. Algorithms based on Region Growing ($RGCT$ and $RGNC$) show greater results between $2 < RDE < 9$ in the histogram thus they will not be taken into account later on in this work. Fig. 10 also demonstrates this fact ($0, 4 < OCE < 0, 95$).

The cause of a high error (many results worth $RDE > 20$ and $OCE = 1$) is that there are centres of ellipses (x_{ec}, y_{ec}) that do not necessarily correspond to nuclei (x_{nc}, y_{nc}) so the discrimination of centres that really correspond to a cell nucleus is shown in the next section. In the case of Fig. 10, values of $OCE \approx 1$ indicate that the centres are detected close to a real core.

2.4. Discrimination between nucleus and no nucleus

In order to discriminate between true and false nuclei, we proceed to consider different features: texture, shape and intensity. The goal is to provide to the classification algorithm as much relevant information as possible. The features are calculated for regions that were obtained to implement the four segmentation methods previously applied. In the calculation of the features used in this work, Gray and RGB colour spaces are considered. All the channels (*gray*, *red*, *green* and *blue*), are used for a total of 4 channels.

For each segmentation result is necessary to identify three regions: R_{int},

14

R_{ext} and R_{rect} where R_{int} is the segmentation result (SR), R_{rect} is the smallest rectangle that encloses R_{int} and $R_{ext} = R_{rect} - R_{int}$ as shown in Fig. 11.
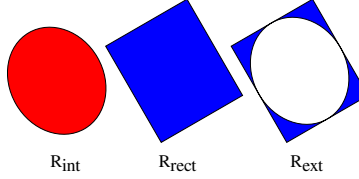

$$R_{int} \qquad R_{rect} \qquad R_{ext}$$

Figure 11: Formation of regions R_{int}, R_{rect} and R_{ext}

For each channel c and R_{int}, 7 features are calculated from the frequency histogram of intensities for a total of 28 features. The total number of features from moments of the R_{int} is 11. The total features from the Gray Level Co-occurrence Matrix (GLCM) (Haralick et al., 1973) is 15 multiplied by 4 (number of channels) in R_{int} that gives a total of 60 characteristics. The intensity and shape features are 4 (one for every channel) and 7 respectively. Finally, the total of calculated features is 110.

The use of texture is a powerful tool for image segmentation but requires the selection of proper features that distinguish the textures in the image for segmentation (Arivazhagan and Ganesan, 2003). The use of texture can be classified as statistical, structural and spectral. Other classification includes wavelets transform, Gabor filters, fractals, mathematical morphology, Markov random fields, feature based interaction maps of pixels and fuzzy logic (Ferreira et al., 2009). Several features have been considered and they are explained below.

2.4.1. Moments

6 spatial moments $(m_{00},\ m_{10},\ m_{01},\ m_{20},\ m_{11},\ m_{02})$, 3 central moments $(cm_{20},\ cm_{11},\ cm_{02})$, the first and second Hu moments $(hum_1,\ hum_2)$ for a total of 11 features in R_{int}. The considered features are shown in Table 1. p is the x-order and q is the y-order, where order means the power component in the sum. $(\overline{x}_{R_{int}}, \overline{y}_{R_{int}})$ is the mass centre of R_{int}.

where I_c is the image I considering only the channel c, R_{int} means internal region, $\eta_{pq,c}$ is the normalized central moment and it is defined as

$$\eta_{pq,c} = \frac{cm_{pq,c}}{m_{00,c}^{(p+q)/2+1}}$$

Spatial moments (p,q) for a channel c	$m_{pq,c} = \sum_{i=1}^{n} I_c(x,y) x^p y^q$
Central moments (p,q) for a channel c	$cm_{pq,c} = \sum_{i=1}^{n} I_c(x,y)(x - \overline{x}_{R_{int}})^p (y - \overline{y}_{R_{int}})^q$
First-order Hu moment for a channel c	$hum_{1,c} = \eta_{20,c} + \eta_{02,c}$
Second-order Hu moment for a channel c	$hum_{2,c} = (\eta_{20,c} - \eta_{02,c})^2 + (\eta_{11,c})^2$

Table 1: Definitions of Spatial Moments, central Moments and Hu Moments

2.4.2. Second order features

Over R_{int} and for each channel c, 15 features are calculated from the Gray Level Co-occurrence Matrix (Haralick et al., 1973): angular second moment (ASM_c), contrast ($Cont_c$), correlation ($Corr_c$), variance (Var_c), inverse difference moment (IDM_c), sum average ($SumAvg_c$), sum variance ($SumVar_c$), sum entropy ($SumEnt_c$), entropy ($Entropy_c$), difference variance ($DiffVar_c$), difference entropy ($DiffEnt_c$), homogeneity ($Homog_c$), inertia ($Iner_c$), dissimilarity ($Diss_c$) and average ($Average_c$). The distance between pixels in order to generate the co-occurrence matrix is equal to one pixel. The features are calculated in four directions (0°, 45°, 90°and 135°) and the results are averaged. The grey levels co-occurrence matrix (GLCM) is a tabulation of how often different combinations of pixel brightness values (grey levels) occur in an image.

From GLCM can be determined 15 features for each channel c (see Table 2).

Some considerations:

- Average and variance calculated using i or j gives the same result, since the GLCM is symmetrical.

- In correlation, μ_x, μ_y, σ_x and σ_y are the mean and standard deviations of p_x and p_y, the partial probability density functions.

- In Sum average, x and y are the coordinates (row and column) of an entry in the GLCM, and $p_{x+y}(i)$ is the probability of GLCM coordinates summing to $x + y$

2.4.3. Shape

The shape features are Circularity (C), Perimeter (P), Equivalent diameter (ED), Eccentricity (E), Major Axis Length ($MaAL$), Minor Axis Length ($MiAL$) as it is mentioned in (Plissiti et al., 2011a). In addition, the count of

Average	$Average_c = \sum_{i,j=0}^{N-1} iP_{i,j} = \mu_i$
Variance	$Var_c = \sum_{i,j=0}^{N-1} P_{i,j}(i - \mu_i)^2$
Angular second moment	$ASM_c = \sum_{i,j=0}^{N-1} P_{i,j}^2$
Contrast	$Cont_c = \sum_{i,j=0}^{N-1}(i-j)^2 P_{i,j}$
Correlation	$Corr_c = \frac{\sum_{i,j=0}^{N-1}(ij)P_{i,j} - \mu_x\mu_y}{\sigma_x\sigma_y}$
Inverse difference moment	$IDM_c = \sum_{i,j=0}^{N-1} P(i,j)\frac{1}{1+(i-j)^2}$
Sum average	$SumAvg_c = \sum_{i=2}^{2N} ip_{x+y}(i)$
Sum variance	$SumVar_c = \sum_{i=2}^{2N}(i - f_s)^2 p_{x+y}(i)$
Sum entropy	$SumEnt_c = -\sum_{i=2}^{2N} p_{x+y}(i)logp_{x+y}(i) = f_s$
Entropy	$Entropy_c = -\sum_{i,j=0}^{N-1} P_{i,j}(logP_{i,j})$
Difference variance	$DiffVar_c = \sum_{i=0}^{N-1} i^2 p_{x-y}(i)$
Difference entropy	$DiffEnt_c = -\sum_{i=0}^{N-1} p_{x-y}(i)logp_{x-y}(i)$
Dissimilarity	$Diss_c = \sum_{i,j=0}^{N-1} P_{i,j}|i-j|$
Homogeneity	$Homog_c = \sum_{i,j=0}^{N-1} \frac{P_{i,j}}{1+(i-j)^2}$
Inertia	$Iner_c = \sum_{i,j=0}^{N-1} P_{i,j}(i-j)^2$

Table 2: GLCM features

sign changes, over the curvature of the object contour, is calculated (CSC) for a total of 7 shape features. The shape features are shown in Table 3.

2.4.4. Intensity

The intensity feature is the Foreground-Background contrast (FBC_c) in the 4 channels for a total of 4 features. Table 4 shows how to calculate the intensity feature for each channel.

$Mean_{R_{ext},c}$ corresponds to the average intensity values in the region R_{ext} for the channel c and $Mean_{R_{int},c}$ is the average intensity values in the region R_{int} for the channel c.

2.4.5. Frequency histogram

For each channel c of the R_{int}, 7 features are detected: Uniformity ($Unif_c$), Entropy (Ent_c), Smoothness ($Smooth_c$), Mean ($Mean_c$), Standard Deviation ($StdDev_c$), Skewness (Skw_c) and Kurtosis ($Kurt_c$). Table 5 shows the features calculated from the frequency histogram for each channel c.

17

Area (A)	Number of pixels belonging to the region R_{int}
Perimeter (P)	Number of pixels belonging to the R_{int} border
Circularity	$C = \frac{4\pi A}{P2}$
Equivalent diameter	$ED = \frac{4A}{\pi}$
Major axis length ($MaAL$)	Corresponds with the greater length of the rectangle with the smallest area that encloses the object of interest.
Minor axis length ($MiAL$)	Correspond with the minor length of the rectangle of the smallest area that encloses the object of interest
Eccentricity	$E = \frac{\sqrt{MaAL-MiAL}}{MaAL}$
Number of curvature sign changes (CSC)	From the curvature sign k which indicates the direction in which the unit tangent vector rotates as a function of the parameter along the contour of the region R_{int}. If the unit tangent rotates counter-clockwise, then $k > 0$. If it rotates clockwise, then $k < 0$. Crossing the boundary of R_{int}, CSC is the number of sign changes of k. $k = \frac{x'y''-y'x''}{\sqrt{(x'^2+y'^2)^3}}$

Table 3: Shape features

Foreground-Background contrast	$FBC_c = Mean_{R_{ext},c} - Mean_{R_{int},c}$

Table 4: Intensity features

2.4.6. Features selection

Feature selection is the process of selecting a subset of features occurring in the training set and using only this subset as features in the classification. Feature selection serves two main purposes: Firstly it makes the processes of training and classification more efficient, by decreasing the size of the data set. Secondly, feature selection often increases classification accuracy by eliminating noise features. A noise feature is one that, when added to the dataset, increases the classification error on new instances (Christopher

18

Mean	$mean_c = Mean_{R_{int},c}$
Standard Deviation	$StdDev_c = \sqrt{\frac{\sum_{x,y \in R_{int}}(I_c(x,y)-mean_c)^2}{A}}$
Skewness	$Skw_c = \frac{mean_c^3}{StdDev_c^3}$
Kurtosis	$Kur_c = \frac{mean_c^4}{StdDev_c^4}$
Uniformity	$Unif_c = \sum_{i=0}^{255} hist_c[i]^2$
Entropy	$Ent_c = \sum_{i=0}^{255} hist_c[i]\log_2(hist_c[i])$
Smoothness	$Smooth_c = \sum_{i=0}^{255}(i - Mean_c)^2 hist_c[i]$

Table 5: Frequency histogram features

D. Manning and Schütze, 2008).

Since four segmentation methods were applied, there is up to total of four data sets (one for each segmentation method) for the extraction of features and future classifier training. 10 fold cross-validation will be used in the experiment. After detecting the centres of the ellipses in the previous step, the resulting regions of each segmentation method will be labelled as nucleus if the ellipse centre corresponds to a real nucleus and with values of $RDE <= 2$ and $OCE <= 1.5$. If the ellipse centre does not correspond with a real nucleus and $RDE > 20$ and $OCE = 1$ this centre will be labelled as no nucleus. For each region, all the features are calculated.

For the selection of the most representative features the Best First Search algorithm (Rich and Knight, 1991) was used. It searches the space of attribute subsets by greedy hill climbing augmented with a backtracking facility. Setting the number of consecutive non-improving nodes allows controlling the level of backtracking done. The best first step may be with the empty set of attributes and then to search the other sets. As evaluator CfsSubsetEval (Hall, 1998) was used, it evaluates the worth of a subset of attributes by considering the individual predictive ability of each feature along with the degree of redundancy between them. Subsets of features that are highly correlated with the class and have low inter-correlation are preferred. They are implemented in Weka software (Hall et al., 2009). Table 6 shows the features selected for each dataset.

2.4.7. Classification

The considered classification algorithms are: Support Vector Machine (SVM) and Artificial Neural Network implemented in (Chang and Lin, 2001) and (Lopez, 2010), respectively.

Dataset	Selected features
FM	$\boldsymbol{Area}$, cm_{11}, $\boldsymbol{hum_1}$, $\boldsymbol{C}$, $\boldsymbol{CSC}$, FBC_{gray}, $SumAvg_{gray}$, $SumVar_{gray}$, $\boldsymbol{Var_{gray}}$, FBC_{red}, $Mean_{green}$, Skw_{green}, $SumAvg_{green}$, Var_{green}, $Mean_{blue}$, $SumVar_{blue}$
GAC	$\boldsymbol{Area}$, $\boldsymbol{hum_1}$, $\boldsymbol{C}$, $\boldsymbol{CSC}$, FBC_{gray}, $Mean_{gray}$, $SumAvg_{gray}$, $\boldsymbol{Var_{gray}}$, FBC_{red}, Skw_{green}, $Mean_{blue}$, Var_{blue}
SD	$\boldsymbol{Area}$, cm_{20}, $\boldsymbol{hum_1}$, $\boldsymbol{C}$, $\boldsymbol{CSC}$, $Mean_{gray}$, $\boldsymbol{Var_{gray}}$, FBC_{red}, $SumAvg_{red}$, $Mean_{blue}$, Ent_{blue}, $SumAvg_{blue}$, Var_{blue}
WS	$\boldsymbol{Area}$, $\boldsymbol{hum_1}$, $\boldsymbol{C}$, $\boldsymbol{CSC}$, $Mean_{gray}$, $SumAvg_{gray}$, $\boldsymbol{Var_{gray}}$, $Mean_{green}$, Skw_{green}, $SumAvg_{blue}$

Table 6: Selected features for each dataset

A support vector machine (SVM) constructs a hyperplane or one set of hyperplanes in a high or infinite dimensional space, which can be used for many tasks like classification or regression. The kernel used is the RBF (see Eq. 8). In order to design the SVM, the input data is initially scaled. Next, using 10 fold cross-validation, the best parameters C and γ are determined. They are used to testing the whole training set. The selected parameters are shown in Table 7.

$$K(x,y) = e^{\gamma ||x-y||^2} \tag{8}$$

	FM	GAC	WS	SD
C	32	32	2	8
γ	0.0078125	0.0078125	0,0078125	8

Table 7: SVM estimated parameter values for each segmentation algorithm

An artificial neural network (ANN) is a mathematical model that is inspired by the structure and/or functional aspects of biological neural networks. A neural network consists of an interconnected group of artificial neurons, and it processes information using a connectionist approach to computation.

The MLP neural network with three layers was used. The first layer has a number or neurons equal to the amount of input variables. The middle layer

has $2 * NC$ neurons, where NC is the number of features used to classify, and the output layer has 2 output neurons (nucleus and no nucleus). The activation functions in the hidden and output layers are hyperbolic tangent and linear respectively. The gradient descent training algorithm is used with the mean squared error as the objective function. The input data is scaled between -1 and 1. 10 fold cross-validation is used again. For each fold, the dataset is divided in 60% for train (its setting depends on this error), 20% to validate as a measure of the widespread network (it allows stopping the training when it is not possible to improve the generalization) and 20% to evaluate without effect in the training process, providing a measure of network performance during and after training. Fig. 12 shows the training evolution of the four neural networks over 500 epochs.
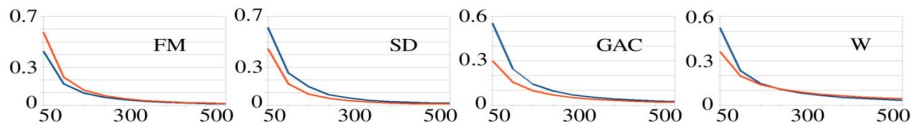

Figure 12: Training evolution of the four neural networks over 500 epochs. In blue the evaluation curve and in red the Validation error.

3. Results

It was found that the centres of detected ellipses always coincide with the centres of the nuclei considered in the Ground True. But also false nuclei are detected. In this paper we assess the accuracy of the classification and the segmentation results with respect to a GT.

3.1. Evaluation of classifiers

In order to evaluate the ANN and the SVM, 10 fold cross-validation is used. The algorithm has to be tested on a sufficiently big dataset. The Hospital Clínico San Cecilio de Granada and Hospital General de Ciudad Real[2] were kind enough to supply us with a database composed of 206 images acquired from 20 different microscope slides. The system used was a Aperio ScanScope, the magnification 40x and the image format lossless compressed tiff . In total, there are 577 nuclei present in the images.

---

[2]We acknowledge the help provided by Doctors Esquivias and Garcia-Rojo.

To evaluate the classifier performance the true positive (TP), true negative (TN), false positive (FP) and false negative (FN) are calculated. The performance measure that was used to evaluate the algorithms was the harmonic mean (HM) of sensitivity and specificity which is defined as:

$$HM = \frac{2 \times Sens \times Spec}{Sens + Spec} \tag{9}$$

Where the sensitivity ($Sens$) and the specificity ($Spec$) are calculated as $Sens = \frac{TP}{TP+FN}$ and $Spec = \frac{TN}{TN+FP}$.

The results obtained by the algorithm can be seen in the table 8. The SVM used in the FM and SD segmentation algorithm has a high HM with the selected features. The ANN used in FM and SD show the same result.

	FM		GAC		WS		SD	
	ANN	SVM	ANN	SVM	ANN	SVM	ANN	SVM
$Sens$	0,9814	0,9816	0,9290	0,8500	0,8445	0,8507	0,9863	0,9766
$Spec$	0,9919	0,9782	0,9826	0,9714	0,9782	0,9668	0,9927	0,9934
HM	**0,9866**	**0,9799**	0,9551	0,9067	0,9064	0,9050	**0,9895**	**0,9850**
% correct	**98,897**	**98,037**	96,989	94,105	93,194	90,009	**99,091**	**98,867**

Table 8: Results obtained by the ANN and the SVM

3.2. Evaluation of the accuracy of the segmentation methods

In order to evaluate the accuracy of the segmentation methods, we use the nuclei correctly classified and the comparison functions OCE and RDE to evaluate each of the results. The results are averaged and shown in Table 9.

Measure Algorithm	WS	GAC	FM	SD
RDE	$3.176 \pm 7,23$	$1,721 \pm 5.51$	$1,053 \pm 3,05$	$\mathbf{0,522 \pm 1,05}$
OCE	$0,199 \pm 0,19$	$0,176 \pm 0,12$	$0.145 \pm 0,07$	$\mathbf{0,121 \pm 0,05}$

Table 9: Segmentation results using the comparison functions OCE and RDE

Finally, a hypothesis test is applied to the comparison functions results, like the wilcoxon matched-pairs signed-ranks test for zero median (Wilcoxon, 1945). This test allows finding if significant difference between any two algorithms exist. The statistical test shows significant differences between the four algorithms using the comparison functions RDE and OCE.

22

In the Fig. 13 and Fig. 14, the black region surrounded by the white contour is the correct classification as nucleus and its segmentation; while the red region surrounded by the white contour is the correct classification as no nucleus and its segmentation result.
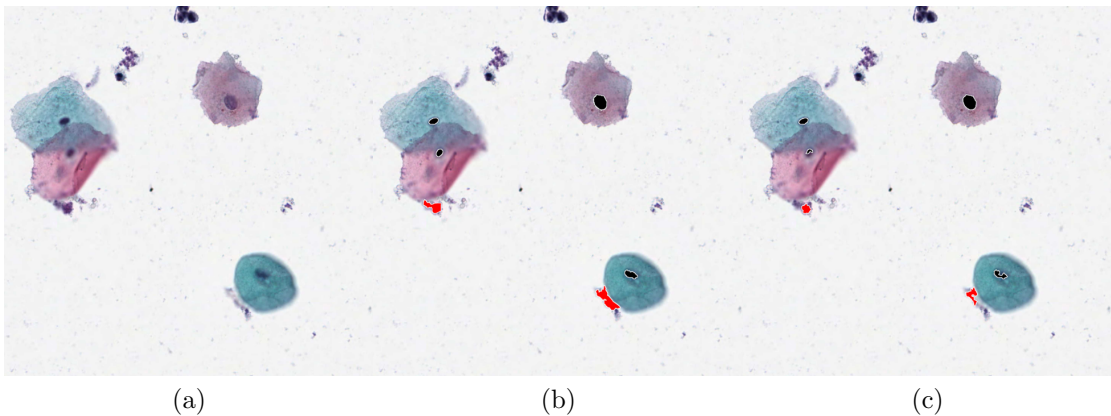

| (a) | (b) | (c) |

Figure 13: (a) Original image. (b) results using GAC. (c) results using WS

4. Conclusions

This work shows an accurate way to detect cervical cell nuclei. The detection of the nuclei and subsequent discrimination of the false nuclei shows a high percentage of correct classifications, up to 98 percent in the case of FM and SD algorithms. In table 6, we noted that there are common attributes selected for each dataset.

An exhaustive study is performed that could be used as reference for all the researchers that need to evaluate the suitability of a classification method to perform the feature extraction. In respect of the possible applications on the expert and intelligent systems field, the detailed study of how to evaluate the suitability of the classification method that needs to be used can be reproduced for other problems. This can also be applied to problems that require feature extraction of the object that needs to be processed. Besides, this works shows a method used to help the expert to improve their performance by diminishing the error possibility.
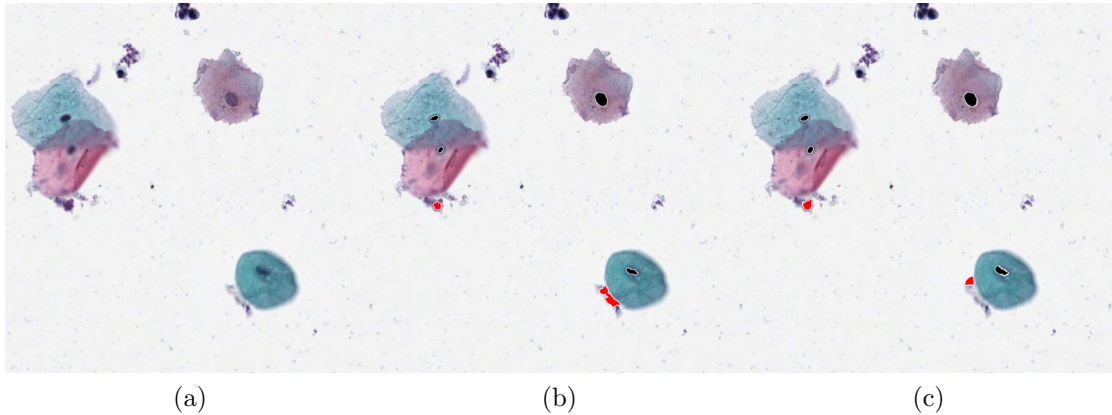
23

Figure 14: (a) Original image. (b) results using FM (c) results using SD

The statistical test application allows validating the results shown in table 9 where the SD algorithm shows the most accurate result according to the comparison functions OCE and RDE. It is followed by FM, GAC and finally the WS algorithm. This kind of study will allow to the researchers interested in this topic to spend less time trying the different algorithms and so, it is an interesting contribution in order to improve the researching in the field.

Finally, the proposal considers the different scales for the analysed data. It allows manipulating the data in the scale where the relation detection/location is better. And so, the segmentation is more accurate.

5. Acknowledgement

References

R. Ali, M. Gooding, T. Szilágyi, B. Vojnovic, M. Christlieb, and M. Brady. Automatic segmentation of adherent biological cell boundaries and nuclei

from brightfield microscopy images. *Machine Vision and Applications*, 23 (4):607–621, 2012. doi: 10.1007/s00138-011-0337-9.

S. Arivazhagan and L. Ganesan. Texture segmentation using wavelet transform. *Pattern Recognition Letters*, 24(16):3197–3203, 2003. ISSN 0167-8655. doi: 10.1016/j.patrec.2003.08.005.

M. Bennasar, Y. Hicks, and R. Setchi. Feature selection using joint mutual information maximisation. *Expert Systems with Applications*, 42(22):8520 – 8532, 2015. ISSN 0957-4174. doi: http://dx.doi.org/10.1016/j.eswa.2015.07.007.

C. Bergmeir, M. García-Silvente, and J. Benítez. Segmentation of cervical cell nuclei in high-resolution microscopic images: A new algorithm and a web-based software framework. *Computer Methods and Programs in Biomedicine*, 107(3):497–512, 2012. doi: 10.1016/j.cmpb.2011.09.017.

J. Canny. Computational approach to edge detection. *IEEE Transactions on Pattern Analysis and Machine Intelligence*, PAMI-8(6):679–698, 1986.

V. Caselles, R. Kimmel, and G. Shapiro. Geodesic active contours. *International Journal on Computer Vision*, 22(1):61–97, 1997.

C.-C. Chang and C.-J. Lin. *LIBSVM: a library for support vector machines*, 2001. Software available at `http://www.csie.ntu.edu.tw/~cjlin/libsvm`.

Y.-T. Chen, P.-C. Huang, and K.-S. Cheng. Cellular image analysis for cervicovaginal smears characterization. In *IEEE EMBS Asian-Pacific Conference on Biomedical Engineering*, pages 206–207, October, 20-22 2003.

P. R. Christopher D. Manning and H. Schütze. *Introduction to Information Retrieval*. Cambridge University Press, 2008. ISBN 0521865719.

S. Colantonio, M. Martinelli, O. Salvetti, I. B. Gurevich, and Y. O. Trusova. Cell image analysis ontology. *Information Technologies for Biomedical and Biotechnical Systems, Pattern Recognition and Image Analysis, Pleiades Publishing, Ltd.*, 18(2):332–341, 2008. ISSN 1054-6618.

D. Comaniciu and P. Meer. Mean shift analysis and applications. In *The Proceedings of the Seventh IEEE International Conference on Computer Vision*, volume 2, pages 1197–1203, September 1999. ISBN 0-7695-0164-8.

M. Farhan, P. Ruusuvuori, M. Emmenlauer, P. Rämö, C. Dehio, and O. Yli-Harja. Multi-scale gaussian representation and outline-learning based cell image segmentation. *BMC Bioinformatics*, 14(SUPPL10), 2013. doi: 10.1186/1471-2105-14-S10-S6.

M. Ferreira, C. Santos, and J. Monteiro. A texture segmentation prototype for industrial inspection applications based on fuzzy grammar. *Sensor Review*, 29(2):163–173, 2009. ISSN 0260-228. doi: 10.1108/02602280910936273.

M. Garcia-Silvente, J. A. Garcia, J. Fdez-Valdivia, and A. Garrido. A new edge detector integrating scale-spectrum information. *Image and Vision Computing*, 15(12):913–923, 1997.

E. A. Gerlein, M. McGinnity, A. Belatreche, and S. Coleman. Evaluating machine learning classification for financial trading: An empirical approach. *Expert Systems with Applications*, 54:193 – 207, 2016. ISSN 0957-4174. doi: http://dx.doi.org/10.1016/j.eswa.2016.01.018.

R. C. González and R. E. Goods. *Digital Image Processing*. Tom Robbins, 2nd edition, 2002. ISBN 0-201-18075-8.

M. Hall, E. Frank, G. Holmes, B. Pfahringer, P. Reutemann, and I. H. Witten. The weka data mining software: An update. *SIGKDD Explorations*, 11(1), 2009.

M. A. Hall. *Correlation-based Feature Subset Selection for Machine Learning*. PhD thesis, University of Waikato, Hamilton, New Zealand, 1998.

R. M. Haralick, K. Shanmugam, and I. Dinstein. Textural features for image classification. *IEEE Transactions on Systems, Man, and Cybernetics*, SMC-3(6):610–621, November 1973.

N. M. Harandi, S. Sadri, N. A. Moghaddam, and R. Amirfattahi. An automated method for segmentation of epithelial cervical cells in images of thinprep. *Journal of Medical Systems*, 34(6):1043–1058, December 2010. ISSN 0148-5598. doi: 10.1007/s10916-009-9323-4.

L. Ibanez, W. Schroeder, L. Ng, and J. Cates. *The ITK Software Guide*, 2003. Available at `http://www.itk.org/ItkSoftwareGuide.pdf`.

S. Inverso. Ellipse detection using randomized hough transform[r]. Technical report, Department of Computer Science, Rochester Institute of Technology, New York, 2002.

K.-B. Kim, S. Kim, and G.-H. Kim. Nucleus classification and recognition of uterine cervical pap-smears using fcm clustering algorithm. *B. Beliczynski et al. (Eds.): ICANNGA 2007, Part II, Lectures Notes in Computer Science 4432, Springer-Verlag Berlin Heidelberg*, pages 290–299, 2007.

L. G. Koss, M. E. Sherman, M. B. Cohen, A. R. Anes, T. M. Darraghi, L. B. Lemos, B. J. McClellan, D. L. Rosenthal, S. Keyhani-Rofagha, K. Schreiber, and P. T. Valente. Significant reduction in the rate of false-negative cervical smears with neural network-based technology (papnet testing system). *Human Pathology*, 28(10):1196–1203, 1997.

N. Lassouaoui, L. Hamami, and N. Nouali. Morphological description of cervical cell images for the pathological recognition. volume 5, pages 49–52, 2005.

K. Li, Z. Lu, W. Liu, and J. Yin. Cytoplasm and nucleus segmentation in cervical smear images using radiating gvf snake. *Pattern Recognition*, 45 (4):1255–1264, 2012. doi: 10.1016/j.patcog.2011.09.018.

C.-H. Lin, Y.-K. Chan, and C.-C. Chen. Detection and segmentation of cervical cell cytoplast and nucleus. *International Journal of Imaging Systems and Technology*, 19(3):260–270, 2009.

R. Lopez. *Flood: An Open Source Neural Networks C++ Library*, 2010. Software available at `http://www.cimne.com/flood/`.

R. Malladi, J. A. Sethian, and B. C. Vermuri. Shape modeling with front propagation: A level set approach. *IEEE Transactions on Pattern Analysis and Machine Intelligence*, 17(2):158–174, 1995.

P. Malm, B. Balakrishnan, V. Sujathan, R. Kumar, and E. Bengtsson. Debris removal in pap-smear images. *Computer Methods and Programs in Biomedicine*, 111(1):128–138, 2013. doi: 10.1016/j.cmpb.2013.02.008.

N. A. Mat-Isa, M. Y. Mashor, and N. H. Othman. An automated cervical pre-cancerous diagnostic system. *Artificial Inteligence in Medicine*, 42(1): 1–11, 2008. doi: 10.1016/j.artmed.2007.09.002.

R. McLaughlin. Randomized hough transform: Improved ellipse detection with comparison. *Pattern Recognition Letters*, 19(3-4):299–305, 1998.

F. Meyer and S. Beucher. Morphological segmentation. *Journal of Visual Communication and Image Representation*, 1(1):21–46, 1990.

L. H. Oliver, R. S. Poulsen, G. T. Toussaint, and C. Louis. Classification of atypical cells in the automatic cytoscreening for cervical cancer. *Patton Recognition, Pcrsamon Press Ltd, Printed in Great Britain*, 11:205–212, 1979.

P.-Y. Pai, C.-C. Chang, and Y.-K. Chan. Nucleus and cytoplast contour detector from a cervical smear image. *Expert Systems with Applications*, 39(1):154 – 161, 2012. ISSN 0957-4174. doi: http://dx.doi.org/10.1016/j. eswa.2011.06.034.

M. Plissiti, C. Nikou, and A. Charchanti. Combining shape, texture and intensity features for cell nuclei extraction in pap smear images. *Pattern Recognition Letters*, 32(6):838–853, 2011a. doi: 10.1016/j.patrec.2011.01. 008.

M. Plissiti, C. Nikou, and A. Charchanti. Automated detection of cell nuclei in pap smear images using morphological reconstruction and clustering. *Information Technology in Biomedicine, IEEE Transactions on*, 15(2):233 –241, march 2011b. ISSN 1089-7771. doi: 10.1109/TITB.2010.2087030.

M. Polak, H. Zhang, and M. Pi. An evaluation metric for image segmentation of multiple objects. *Image and Vision Computing*, 27(8):1223–1227, 2009. ISSN 0262-8856. doi: 10.1016/j.imavis.2008.09.008.

E. Rich and K. Knight. *Artificial Intelligence*. McGraw-Hill, 1991.

C. Sagiv, N. A. Sochen, and Y. Y. Zeevi. Integrated active contours for texture segmentation. *IEEE Transactions on Image Processing*, 15(6): 1633–1646, 2006. doi: 10.1109/TIP.2006.871133.

P. Sobrevilla, E. Montseny, and E. Lerma. A fuzzy-based automated cells detection system for color pap smear tests -facsds-. *Fuzzy Sets and Their Extensions: Representation, Aggregation and Models. H. Bustince et al., (eds.). Springer 2008*, pages 657–674, 2008.

F. Vaschetto, E. Montseny, P. Sobrevilla, and E. Lerma. Threecond: An automated and unsupervised three colour fuzzy-based algorithm for detecting nuclei in cervical pap smear images. In *Proceedings of the 2009 Ninth International Conference on Intelligent Systems Design and Applications*, ISDA '09, pages 1359–1364, Washington, DC, USA, 2009. IEEE Computer Society. ISBN 978-0-7695-3872-3.

F. Wilcoxon. Individual comparisons by ranking methods. *Biometrics Bulletin*, 1(6):80–83, December 1945.

WorldHealthOrganization. Comprehensive cervical cancer control: a guide to essential practice. Technical report, World Health Organization, Department of Reproductive Health and Research and Department of Chronic Diseases and Health Promotion, New York, 2006.

L. Xu, E. Oja, and P. Kultanena. A new curve detection method: Randomized hough transform (rht). *Pattern Recognition Letters*, 11(5):331–338, 1990.

S.-F. Yang-Mao, Y.-K. Chan, and Y.-P. Chu. Edge enhancement nucleus and cytoplast contour detector of cervical smear images. *IEEE Transactions on Systems, Man, and Cybernetics, Part B: Cybernetics*, 38(2):353–366, 2008. doi: 10.1109/TSMCB.2007.912940.

L. Zhang, H. Kong, C. Chin, T. Wang, and S. Chen. Cytoplasm segmentation on cervical cell images using graph cut-based approach. *Bio-Medical Materials and Engineering*, 24(1):1125–1131, 2014. doi: 10.3233/BME-130912.